Nano Research

Enhanced dual plasmonic photocatalysis through plasmonic coupling in eccentric noble metal–nonstoichiometric copper chalcogenide hetero-nanostructures

Mariia Ivanchenko[1], Vida Nooshnab[2], Alline F. Myers[3], Nicolas Large[2], Andrew J. Evangelista[1], and Hao Jing[1] (✉)

[1] Department of Chemistry and Biochemistry, George Mason University, Fairfax, Virginia 22030, USA
[2] Department of Physics and Astronomy, The University of Texas at San Antonio, San Antonio, TX 78249, USA
[3] National Institute of Standards and Technology (NIST), 100 Bureau Dr., Gaithersburg, Maryland 20899, USA

ABSTRACT
The extension of plasmonics to materials beyond the conventional noble metals opens up a novel and exciting regime after the inspiring discovery of characteristic localized surface plasmon resonances (LSPRs) in doped semiconductor nanocrystals originating from the collective oscillations of free holes in the valence band. We herein prepare colloidal monodisperse eccentric dual plasmonic noble metal-nonstoichiometric copper chalcogenide ($Au@Cu_{2-x}Se$) hybrid hetero-nanostructures with precisely controlled semiconductor shell size and two tunable LSPRs in both visible (VIS) and near-infrared (NIR) regions associated with Au and $Cu_{2-x}Se$, respectively. Through systematic evaluations of the photocatalytic performance of $Au@Cu_{2-x}Se$ upon sole NIR and dual VIS + NIR simultaneous excitations, we are capable of unambiguously elucidating the role of plasmonic coupling between two dissimilar building blocks on the accelerated photocatalytic reactions with greater rate constants from both experimental and computational perspectives. The significantly enhanced strength of the electromagnetic field arising from efficient plasmonic coupling under the excitation of two LSPRs results in the superior activities of dual plasmonic $Au@Cu_{2-x}Se$ in photocatalysis. The new physical and chemical insights gained from this work provide the keystone for the rational design and construction of high-quality dual- or even multi-plasmonic nano-systems with optimized properties for widespread applications ranging from photocatalysis to molecular spectroscopies.

1   Introduction

The burgeoning research field of plasmonics based on localized surface plasmon resonances (LSPRs) in noble metals, especially gold, silver, and copper nanoparticles, has now been well-established since the intriguing optical properties of the Lycurgus cup due to the nanoscopic plasmonic particles embedded in the glass [1–7]. However, LSPRs were not specific only to noble metal nanostructures [8]. Instead, they are being recognized more generally as ubiquitous optical signatures of charge carriers [9]. The extension of plasmonics to materials beyond the noble metals was realized after the inspiring discovery of LSPRs in doped semiconductor nanocrystals, such as binary metal chalcogenides [10–20], oxides [21–26], nitrides [27, 28], phosphides [29], and silicon [30]. This ushers in a novel and exciting regime in plasmonics of nonmetallic nanostructures. In striking contrast to their metallic analogues whose LSPRs originate from the collective oscillations of free electrons in the conduction band, the LSPRs in these doped semiconductor nanoparticles essentially arise from the collective oscillation of free holes in the valence band [31]. Among those plasmonic doped semiconductor nanocrystals, p-type nonstoichiometric

copper chalcogenides ($Cu_{2-x}E$, $x > 0$, E = S, Se, Te) exhibiting stoichiometry-dependent bandgaps [32, 33] are the most studied and extensively exploited materials for plasmonic-based applications. Nonstoichiometric copper chalcogenides possess superior capabilities in controlling of LSPRs, which are otherwise not readily accessible through dopant-dependent phase transformation and ligand exchange in their n-type counterparts, such as plasmonic metal oxides (e.g., In_2O_3, MoO_3, WO_3) [31, 34]. Due to the lower carrier (positively charged holes) density (on the order of 10^{21} cm^{-3}) than those in noble metals (10^{22} cm^{-3} to 10^{23} cm^{-3}), LSPRs of heavily-doped copper chalcogenides are located within the near-infrared region (800 nm to 2,000 nm). Fundamentally distinct from the static nature of the optical resonances of noble metals that are sensitively dependent upon the geometrical parameters [35–44], the tunability of LSPRs in copper chalcogenides is uniquely dynamic as the plasmonic properties can be post-synthetically modified *in situ* by redox doping or electrochemically charging and discharging [13, 14, 45–48]. Owing to the unique and distinct characteristics in LSPRs, the integration of noble metals and nonstoichiometric copper chalcogenides to form structurally well-defined dual plasmonic hybrid hetero-nanostructures

with synergistically reinforced optical features can be an ideal platform to systematically investigate the electronic interactions of two intrinsically dissimilar constituent domains at the nanoscale [49, 50]. This in turn helps us gain tremendous insights into more fundamental questions such as how the energy transfer and local plasmonic field are modulated by the nanoscale interactions between the two different plasmonic building blocks [51, 52]. Although great strides have been achieved in the past few years, the majority of the work is focused on biomedical areas, such as multimodal bioimaging [53–55], and photothermal and photodynamic cancer therapy [56–59]. The emergence of photocatalysis driven by plasmonic coupling on dual plasmonic nano-systems has gradually become a fundamentally important yet unexplored area with numerous open questions well-worthy of systematic and in-depth investigations. Only a few reports about the role of plasmonic coupling in photocatalysis using core-shell dual plasmonic nanostructures have been published [60, 61]. However, to the best of our knowledge, the comparisons and evaluations of photocatalytic efficacies in the same dual plasmonic nanostructure under sole near infrared (NIR) excitation of optical resonances of shelling copper chalcogenides and simultaneous visible (VIS) and NIR excitations of LSPRs for both noble metal and copper chalcogenides are still lacking. This knowledge gap inevitably results in ambiguous conclusions on the intrinsic performances in photocatalysis. Moreover, the mechanisms proposed [60, 61] so far underpinning the experimentally measured photocatalytic activities, such as the enhanced local electromagnetic field induced by plasmonic coupling, are lacking simulation support, which impedes the rational design of efficient photocatalysts based on dual plasmonic nanostructures.

In the present work, we focus on eccentric dual plasmonic core-shell Au@Cu$_{2-x}$Se hetero-nanostructures with precisely tunable plasmonic properties fabricated via a facile and robust selenium-mediated two-step synthesis. The contact between the noble metal and copper chalcogenide due to the complete encapsulation of the Au core within the Cu$_{2-x}$Se shell through designed colloidal synthesis facilitates the plasmonic energy transfer upon the excitations of optical resonances. Photocatalytic decolorization of Rhodamine B in the presence of dual plasmonic Au@Cu$_{2-x}$Se is obtained experimentally when LSPRs of Au core and Cu$_{2-x}$Se shell are simultaneously photoexcited under illumination of a xenon lamp as the light source. Only LSPRs of Cu$_{2-x}$Se are excited after utilizing a NIR cut-off filter (> 760 nm), enabling us to compare their photocatalytic activities under two distinct circumstances. Thus, this permits the elucidation of the role of plasmonic coupling from the experimental perspectives. Computational electrodynamic modeling using the finite-difference time-domain (FDTD) method provides us with the unique spatial distribution of local electric field enhancement along the interface of eccentric dual plasmonic Au@Cu$_{2-x}$Se nanoparticles. Modeling performed under sole and dual excitations of LSPRs further substantiates our experimental results and reveals the effect of plasmonic coupling as well as enhanced local field between Au and Cu$_{2-x}$Se on photocatalysis.

2   Experimental

2.1   Materials

Hexadecyltrimethylammonium bromide (CTAB, > 98.0%), hexadecyltrimethylammonium chloride (CTAC, > 95.0%), hydrogen tetrachloroaurate (III) trihydrate (HAuCl$_4$·3H$_2$O, 99.99%), L-ascorbic acid (AA ≥ 99.0%), sodium borohydride (NaBH$_4$, 99.99%), selenium dioxide (≥ 99.9%), copper (II)

sulfate (99.99%), and Rhodamine B (≥ 95%) were used as received without further purification. The deionized water used in the experiments was ultra-pure (18.2 MΩ resistivity).

2.2   Synthesis of gold nanospheres

Three steps were included in the protocol:

Step 1, cluster solution preparation. 0.6 mL of freshly prepared 0.01 mol/L NaBH$_4$ ice-cold aqueous solution was rapidly injected in a mixture of 0.25 mL of 0.01 mol/L HAuCl$_4$ and 9.75 mL of 0.1 mol/L CTAB aqueous solutions under vigorous stirring. Immediate color change from yellow to light brown was observed. After stirring for one minute at 126 rad/s (1,200 rpm), the solution was left undisturbed for 3 h to allow remaining NaBH$_4$ to decompose.

Step 2, seed solution preparation. 0.1 mmol/L of prepared Au clusters were mixed with 4 mL of 0.2 mol/L CTAC and 3 mL of 0.1 mol/L AA aqueous solutions. Then, 4 mL of 0.5 mmol/L HAuCl$_4$ was rapidly added, and the mixture was stirred for 15 min at room temperature. Au nanoparticles (NPs) seeds were washed twice with water and finally redispersed in 2 mL of 0.02 mol/L CTAC for further use.

Step 3, growth solution. 20 mL of 0.1 mol/L CTAC and 1.3 mL of 0.02 mol/L AA aqueous solutions were mixed with 0.35 mL of seed solution in a 100 mL round bottom flask, followed by dropwise addition of 20 mL of 1 mmol/L HAuCl$_4$ using a syringe pump at an injection rate of 20 mL/h. The reaction was allowed to continue for 10 min after the injection had been finished. Obtained Au NPs were washed by centrifugation at ≈ 29,400 m/s^2 (3,000×g) relative centrifugal field (RCF) for 10 min. After the removal of the supernatant, the product was redispersed in 10 mL of water.

2.3   Synthesis of Au@Cu$_{2-x}$Se nanocrescents

0.25 mL as prepared Au nanospheres were diluted with 1.25 mL of water and mixed with 0.5 mL of 0.02 mol/L CTAC and 0.2 mL of 0.1 mol/L AA aqueous solutions at 40 °C. While stirring at 126 rad/s (1,200 rpm), 5, 10, 20, 50, 75, 100, or 130 μL of 0.01 mol/L SeO$_2$ aqueous solution was added dropwise utilizing a syringe pump with an injection rate of 10 μL/min. The reaction was allowed to proceed for 10 min after the injection had been finished. Then, the Au@Se dispersion was washed twice with water to remove any free Se NPs and redispersed in 2 mL of 5 mmol/L CTAC. 15 μL of 0.2 mol/L CuSO$_4$ and 0.2 mL of 0.1 mol/L AA aqueous solutions were added into the colloid simultaneously at room temperature. The mixture was left under vigorous stirring at 126 rad/s (1,200 rpm) for 40 min. The resulting products were purified through centrifugation at 419 rad/s (4,000 rpm) for 5 min and redispersed in water. The Au@Cu$_{2-x}$Se dispersion was stable at room temperature for more than a month.

2.4   Synthesis of pristine Cu$_{2-x}$Se nanoparticles

Synthesis of pristine Cu$_{2-x}$Se was performed following the same procedure as formation of nanocrescents but fabricated in absence of Au core NPs. 2 mL of 0.005 M CTAC were mixed with 0.2 mL of 0.1 M AA aqueous solutions at 40 °C. While stirring at 1,200 rpm, 50 μL of 0.01 M SeO$_2$ aqueous solution was added dropwise utilizing a syringe pump with an injection rate of 10 μL/min. The formation of Se NPs was allowed to proceed for 10 min after the injection had been finished. 15 μL of 0.2 M CuSO$_4$ and 0.2 mL of 0.1 M AA aqueous solutions were added into the colloid simultaneously at room temperature. The mixture was left under vigorous stirring at 1,200 rpm for 40 min. The resulting products were purified through centrifugation at 6,000 rpm for 5 min and redispersed in water.

2.5   Characterization and instrumentation

Transmission electron microscopy (TEM) images, high-resolution TEM (HRTEM) images, high-angle annular dark-field scanning TEM (HAADF-STEM) images, and energy dispersive X-ray spectroscopy (EDX) measurements were obtained on an analytical transmission electron microscope operating at 300 kV. The TEM samples, including Au@Se and Au@Cu$_{2-x}$Se were prepared by dropping solutions of nanoparticles onto the surface of 300-mesh carbon-coated copper (Cu) grids. Carbon-coated molybdenum (Mo) grids were used for EDX characterization of Au@Cu$_{2-x}$Se nanoparticles to avoid the interference of peaks from the Cu grid. The optical extinction spectra of colloidal nanoparticles were recorded at room temperature on a spectrophotometer equipped with an integrating sphere.

2.6   Electrodynamic modeling of the dual plasmonic properties

Electrodynamic simulations were performed using a commercial solver with the FDTD method. The simulation domain was defined with a size of 0.5 μm × 0.5 μm × 2 μm with perfectly matched layers (PMLs, 32 layers) as boundary conditions in all directions. The Au@Cu$_{2-x}$Se core-shell nanoparticles were discretized with a cubic mesh of 0.75 nm. The optical excitation was modeled as an incident plane-wave (total-field scattered-field source) arriving at normal incidence with the polarization along the symmetry axis of the nanoparticles. In each simulation, the electromagnetic fields were propagated for about 60 fs to ensure the full convergence of the calculated fields. The complex dielectric permittivity of gold was taken from experimentally measured Johnson and Christy constants [62], and the complex permittivity of Cu$_{2-x}$Se was described by a Drude model:

$$\varepsilon_1 = \varepsilon_\infty - \frac{\omega_p^2}{\omega^2 + \gamma^2} \tag{1}$$

$$\varepsilon_2 = \frac{\omega_p^2 \gamma}{\omega(\omega^2 + \gamma^2)} \tag{2}$$

where ε_∞ is the high-frequency dielectric permittivity due to the interband transitions, and $\omega_p = \sqrt{Ne^2/\varepsilon_0 m^*}$ and γ are the plasma frequency of free carriers and the free carrier damping, respectively. The free carrier density is $N = 4.05 \times 10^{21}$ cm^{-3}

and m^* is the charge carrier effective mass [51]. The surrounding medium was modeled with a constant refractive index of 1.46.

2.7   Photocatalytic experiment

The photocatalytic activity of the Au@Cu$_{2-x}$Se nano-crescents with various shell thickness was evaluated by the photo-degradation of Rhodamine B (RhB) under a Xe lamp irradiation equipped with an ultraviolet-cut ($\lambda > 420$ nm) or visible light long pass ($\lambda > 760$ nm) filter at 24 °C. Photocatalytic reactions were conducted in a cylindrical quartz reactor equipped with the outer shell for water circulation. 5 mmol/L solution of RhB was added to 0.25 mL of Au@Cu$_{2-x}$Se dispersion to get a total volume of 2 mL. Prior to illumination, the mixture was magnetically stirred in the dark for 1 h to allow for RhB molecules adsorption onto the catalyst surface. At irradiation time intervals of 30 min, dispersion was collected and centrifuged (419 rad/s (4,000 rpm) for 5 min) to remove the photocatalyst particles. After the catalyst was separated, the ultraviolet (UV) spectrum of the supernatant was recorded. Then, nano-crescents were redispersed in the supernatant and illuminated again. During the photodegradation process, the RhB concentration was monitored by measuring the peak value at 553 nm.

3   Results and discussion

A selenium-mediated two-step synthesis was used to prepare colloidal eccentric dual plasmonic Au@Cu$_{2-x}$Se nanostructures. In the first step, Se was obtained by chemical reduction of SeO$_2$ with the ascorbic acid, penetrated to the surface of Au NPs, and partially replaced molecules of stabilizer. The preferential coating and the growth of Se on one side of uniform CTAC-stabilized Au NPs (average size of ≈ 65 nm) is explained by the shielding effect of the surfactant molecules. Relatively strong blocking of the Au NPs surface sites facilitates deposition of subsequent layers of growth material on previously nucleated Se. The asymmetric growth of the Se shell was clearly demonstrated in TEM images with different magnifications (Figs. 1(a)–1(h), and Fig. S1 in the Electronic Supplementary Material (ESM)). This hetero-nucleation of various amounts of Se allowed us to fabricate Au@Se with controllable Se shell sizes by changing the concentration of selenium precursor SeO$_2$ (Figs. 1(b)–1(h)). The amorphous nature of the selenium (Se) layer was confirmed by the Thon ring pattern obtained from
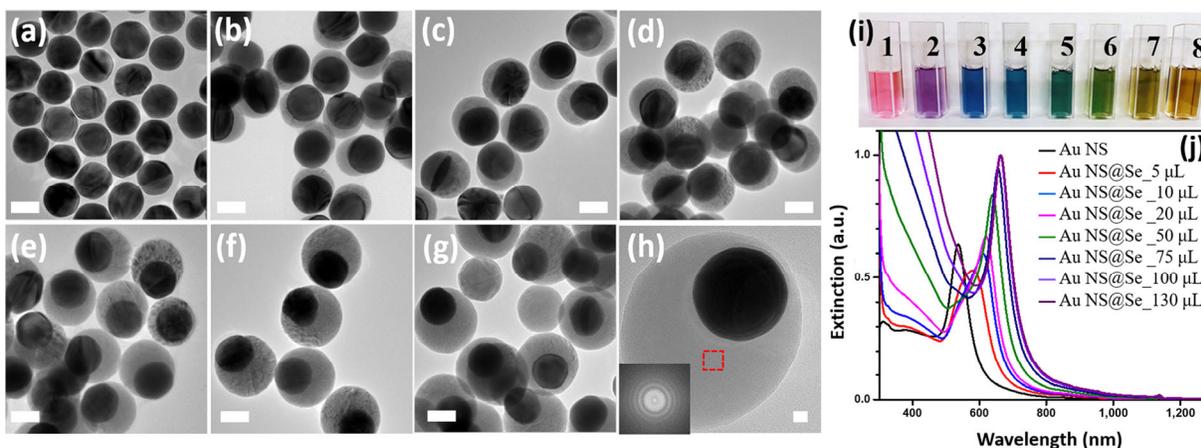
Figure 1   Characterization of eccentric Au@Se nanoparticles. (a) TEM image of Au nanospheres (NS). (b)–(h) TEM images of eccentric Au@Se nanoparticles with increasing Se shell size obtained using (b) 5 μL, (c) 10 μL, (d) 20 μL, (e) 50 μL, (f) 75 μL, (g) 100 μL, and (h) 130 μL of 0.01 mol/L SeO$_2$. The inset image of panel (h) is FFT pattern of the red dashed line square, indicating the absence of crystallinity in Se. Scale bars on (a)–(g) are 50 nm and on (h)– to 10 nm. (i) Ambient light photograph of aqueous solutions of (1) Au and eccentric Au@Se nanoparticles obtained by addition of (2) 5 μL, (3) 10 μL, (4) 20 μL, (5) 50 μL, (6) 75 μL, (7) 100 μL, and (8) 130 μL of 0.01 mol/L SeO$_2$ (cuvette length is 1 cm). (j) UV–vis–NIR extinction spectra of aqueous solutions of Au and eccentric Au@Se nanoparticles synthesized with various amounts of 0.01 mol/L SeO$_2$.

the fast Fourier transform (FFT) image shown in the inset of Fig. 1(h), which is consistent with published results [50, 51]. The color of the colloidal solutions changing from bright purple to vivid greenish yellow was observed as the Se shell size increases (Fig. 1(i)). The increase in Se shell size was accompanied by a damping extinction intensity and a gradual bathochromic shift of intensified LSPRs peaks in the UV–vis–NIR spectra, which was caused by the insufficient electronic interactions between Au and amorphous Se and the remarkably larger refractive index of Se than that of the water medium, respectively (Fig. 1(j)). The photograph in Fig. 2(i) showed that the color of the reaction solutions changed from purple to bluish green after the conversion of Au@Se to Au@Cu$_{2-x}$Se was complete. During the transformation, Cu^{2+} ions were added to the solution of Au@Se containing CTAC and ascorbic acid and reduced to monovalent Cu$^+$ before being incorporated into the Se sublattice to form Cu-deficient Cu$_{2-x}$Se upon the exposure to air for oxidation. TEM images with different magnifications (Figs. 2(a)–2(h), and Fig. S2 in the ESM) depicted the monodispersed eccentric Au@Cu$_{2-x}$Se nanostructures with narrow size distributions. Although the shapes of Au@Cu$_{2-x}$Se remained quite similar to those of intermediate Au@Se nanoparticles, the semiconductor shell of the former was highly crystalline, as unveiled by the representative high-resolution

TEM image (Fig. 3(a)). The change is explained by incorporation of Cu-ions during the reaction and formation of more organized structure with long-range order. The complete encapsulation of Au by Cu$_{2-x}$Se in an asymmetric manner was clearly shown in the image of HAADF-STEM since it is extremely sensitive to variations in the atomic number of atoms in the sample, as shown in Fig. 2(h). Dual plasmonic Au@Cu$_{2-x}$Se exhibited two characteristic LSPR bands in the optical extinction spectra (Fig. 2(j)). The extinction peak centered around 900 nm corresponds to the plasmonic oscillations of free holes in the Cu$_{2-x}$Se, whereas the plasmonic resonance band of Au is in the visible region. In addition to the increasingly strong light absorption at wavelengths below 500 nm induced by intrinsic electronic inter-band transitions from the valence band to the conduction band of Cu$_{2-x}$Se, the progressive red-shift of the Au LSPR from ≈ 530 nm to ≈ 594 nm was noted as the Cu$_{2-x}$Se size increased, which was ascribed to the larger refractive indices. The red-shift of Cu$_{2-x}$Se LSPRs equivalent to the decrease in the energy of plasmonic resonances was attributed to the lower degree of copper deficiency in the larger semiconductor shells [63]. Also, the plasmonic bands of Cu$_{2-x}$Se became more pronounced relative to those of Au due to the increasing of the NIR extinction cross-section as the dimension of the semiconductor expanded (Fig. 2(j)).
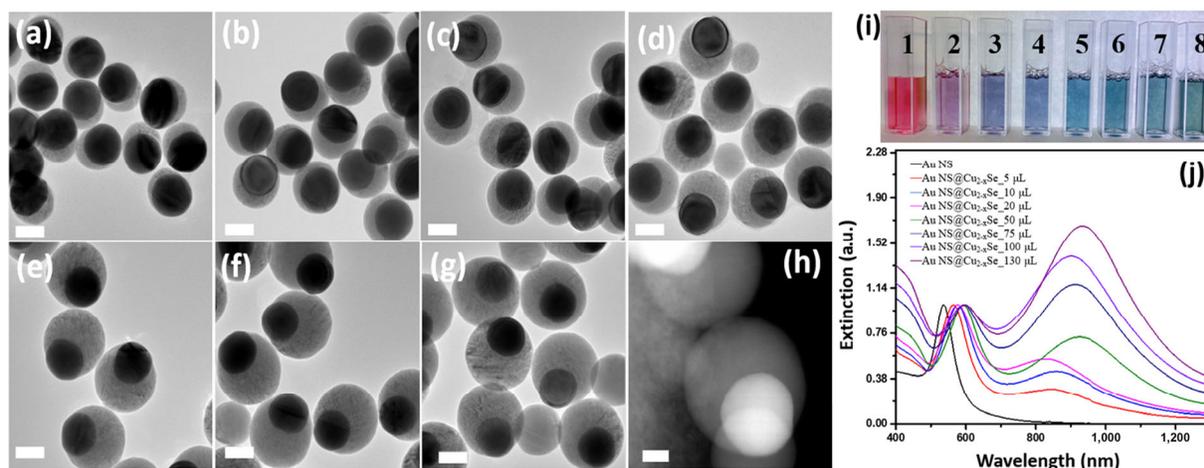
Figure 2 Characterization of eccentric Au@Cu$_{2-x}$Se nanoparticles. (a)–(g) TEM images of eccentric Au@Cu$_{2-x}$Se nanostructures with increasing Cu$_{2-x}$Se shell size obtained from the conversion of Au@Se shown in Figs. 1(b)–1(h). Scale bars correspond to 50 nm. (h) HAADF-STEM image of Au@Cu$_{2-x}$Se obtained from the Au@Se samples using 75 μL of 0.01 mol/L SeO$_2$. Scale bar is 20 nm. (i) Ambient light photograph of aqueous solutions of (1) Au and eccentric Au@Cu$_{2-x}$Se nanoparticles obtained from the conversion of Au@Se shown in Figs. 1(b)–1(h) (cuvette length is 1 cm). (j) UV–vis–NIR extinction spectra of aqueous solutions of Au and eccentric Au@Cu$_{2-x}$Se nanoparticles after the transformation of Au@Se.
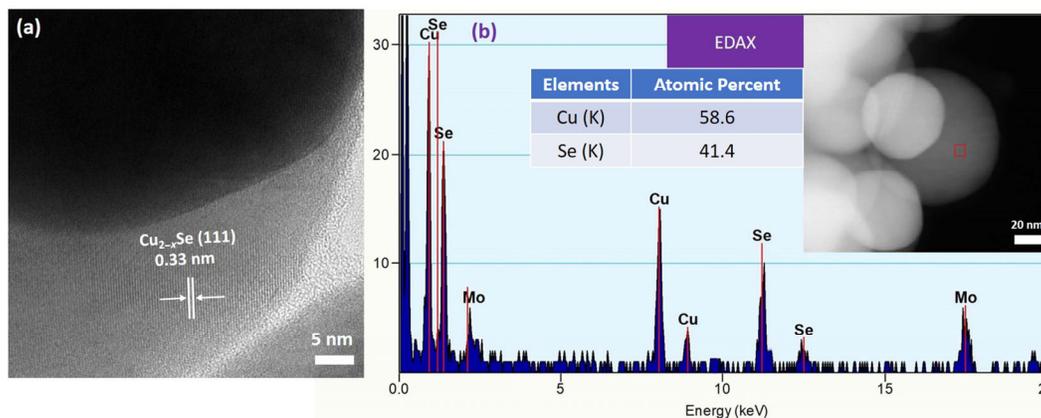
Figure 3 Characterization of Cu$_{2-x}$Se shell. (a) HRTEM image of a Au@Cu$_{2-x}$Se nanoparticle with denoted interplanar spacing corresponding the lattice fringes of the (111) plane of the Cu$_{2-x}$Se domain. The interplanar spacing value is 0.33 nm with standard deviation of 0.010 nm based on 10 measurements of FFT on the sample nanoparticle. (b) The EDX spectrum obtained from the sample synthesized adding 75 μL of 0.01 mol/L SeO$_2$ deposited on Mo grid. The red rectangle in the inset image shows the selected area for EDX inspection. The atomic percentages of Cu (K) and Se (K) are 58.6 ± 3.4 and 41.4 ± 3.8, respectively.

The interplanar spacing measured from high-resolution TEM (HRTEM) image was determined to be 0.33 nm with a standard deviation of 0.01 nm corresponding to the (111) plane of the highly crystalline $Cu_{2-x}Se$ shell (Fig. 3(a)) [64]. The mean and standard deviation values were obtained from the table of d-spacing measurements as shown in Table S3 in the ESM. Furthermore, the STEM-EDX spectrum confirmed the presence of Cu and Se in the outer layer of the hybrids and enabled us to determine the atomic ratio of Cu to Se and the degree of copper deficiency equivalent to x. The EDX spectrum was acquired and quantified using the TEM Imaging and Analysis software on the TEM. The Cu and Se K-lines were used for a standardless quantification. The value of $x = 0.58$ was obtained for the examined sample (Fig. 3(b)). The uncertainty is one standard deviation statistical uncertainty obtained from the EDX data in Fig. 3(b).

The hybrid hetero-nanostructures of $Au@Cu_{2-x}Se$ with various shell thicknesses are expected to possess different x values since the plasmonic features of $Cu_{2-x}Se$ nanocrystals are intimately connected to the Cu to S stoichiometry, that is, Cu deficiency or vacancy doping in the crystalline lattices. The x values of three other samples including $Au@Cu_{2-x}Se$_10 μL, $Au@Cu_{2-x}Se$_50 μL, and $Au@Cu_{2-x}Se$_100 μL were determined to be 0.72, 0.56, and 0.60, respectively based on the atomic ratios of Cu (K) to Se (K) in the EDX spectra (Fig. S14 in the ESM). The decreased x values corresponding to the lowered degree of Cu deficiencies were in good agreement with the red-shift in LSPRs of $Au@Cu_{2-x}Se$ nanostructures in the extinction spectra. The slight blue-shift of LSPRs in the NIR region for $Au@Cu_{2-x}Se$_50 μL and $Au@Cu_{2-x}Se$_100 μL samples was ascribed to the increased x values (from 0.56 to 0.60).

The kinetics of decolorization of RhB can be simply and accurately analyzed using time-resolved UV–vis absorption spectroscopy as the photocatalytic decomposition occurs between RhB and hydroxyl radicals ($\cdot$OH) as an elementary reaction (Figs. S4 and S5 in the ESM). With the assumption of a steady concentration of $\cdot$OH radicals, the rate law as shown below could be well-described as a pseudo-first-order reaction.

$$-\ln\frac{[\text{RhB}]}{[\text{RhB}]_0} = -\ln\frac{I}{I_0} = kt \qquad (3)$$

where $[\text{RhB}]_0$ and $[\text{RhB}]$ are the initial concentration and the concentration of rhodamine B molecules at a reaction time (t), respectively. I_0 and I are the initial intensity and intensity of the absorption peaks at 553 nm at a reaction time (t), respectively. k is the apparent first order rate constant and could be determined by performing least-square curve fitting to the temporal evolution of $-\ln(I/I_0)$ with a linear equation since the concentration is directly proportional to the intensity of the absorption peak at 553 nm.

First, we compared the photocatalytic activities of $Au@Cu_{2-x}Se$ with varied semiconductor shell sizes synthesized by varying the amounts of SeO_2. As shown in Fig. 4(a), illumination of the reaction mixtures utilizing light with wavelengths longer than 760 nm by which only LSPRs of $Cu_{2-x}Se$ in the NIR spectral region were photoexcited drastically accelerated the decolorization process as the size of $Cu_{2-x}Se$ increased, which was further substantiated by the increasing value of the rate constant, k, as indicated in the inset. The similar trend in the photocatalytic behaviors under sole excitation was observed in the same system when both LSPRs of Au and $Cu_{2-x}Se$ were excited (equivalent to dual excitations of VIS and NIR) using an alternative long-pass optical filter with cut-off wavelengths of 420 nm, as demonstrated in Fig. 4(c). The concentrations of colloidal dual plasmonic $Au@Cu_{2-x}Se$ nanoparticles were all kept the same in the comparative studies and the incident optical power densities under sole and dual excitations were precisely tuned to be identical ($\approx$ 200 mW/cm²) determined
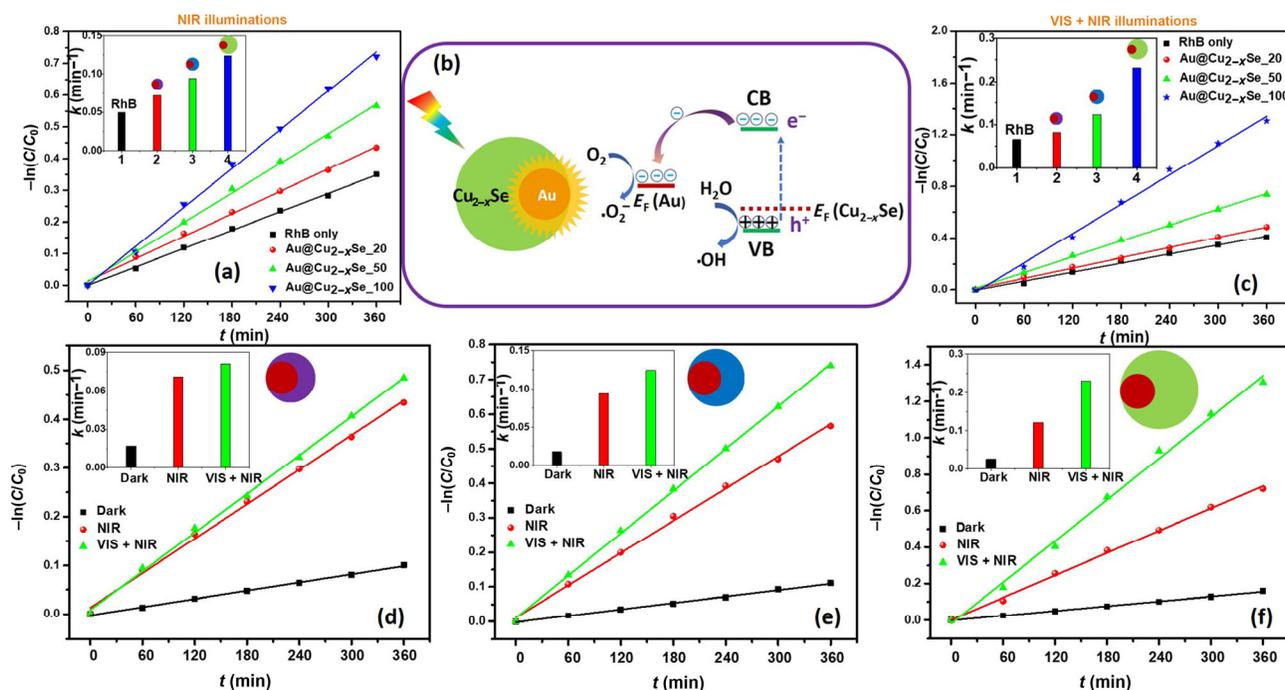
Figure 4 Photocatalytic degradation of RhB on eccentric $Au@Cu_{2-x}S$ nanoparticles. (a) First-order kinetics for RhB degradation under NIR illumination ($\lambda > 760$ nm) using $Au@Cu_{2-x}Se$ nanoparticles of various shell thickness as catalysts. (b) The mechanism illustration of RhB photocatalytic degradation on $Au@Cu_{2-x}Se$ nanoparticles. (c) First-order kinetics for RhB degradation under visible and NIR illumination ($\lambda > 420$ nm) using $Au@Cu_{2-x}Se$ nanoparticles of various shell thickness as catalysts. Insets illustrate the values of rate constants of corresponding reactions in the absence and presence of $Au@Cu_{2-x}Se$ with 3 different shell thicknesses. The standard errors of the slopes for all linearly fitted curves are listed in Figs. S4 and S5 in the ESM. (d)–(f) First-order linear transformations, $-\ln(C/C_0)$, for RhB degradation reactions in the dark, under IR, and both, (visible and IR), illumination in the presence of $Au@Cu_{2-x}Se$ synthesized using (d) 20 μL, (e) 50 μL, and (f) 100 μL of 0.01 mol/L SeO_2. The insets are the comparisons of the kinetic constants (k) of dual plasmonic nanoparticles under different excitation conditions.

by an optical power meter. The photothermal effect was suppressed since the colloidal reaction mixtures were vigorously stirred and the temperature was maintained at 24 °C during the entire process by circulating water in the quartz photo-reactor to facilitate the rapid heat dissipation. The accelerated photocatalytic reaction rates under sole and dual excitations are mainly ascribed to higher amounts of materials in the $Cu_{2-x}Se$ shell and the larger surface area of dual plasmonic nanoparticles.

Secondly, we systematically evaluated the temporal evolution of $-\ln([RhB]/[RhB]_0)$ during photocatalytic degradation on eccentric dual plasmonic nanoparticles with three distinct shell thickness under 3 conditions: darkness, sole excitation of $Cu_{2-x}Se$ NIR LSPRs, and dual VIS + NIR simultaneous excitation of LSPRs for Au and $Cu_{2-x}Se$, as shown in Figs. 4(d)–4(f). In contrast to the kinetically slow reactions in darkness, the molecule-transforming processes were accelerated by excitations. An increasing trend in the values of rate constants was observed as illustrated in the insets of Figs. 4(d)–4(f). With dual excitation the photocatalytic reaction rate is higher than with sole NIR excitation. k of dual excitation is larger than k of sole excitation and grows as the $Cu_{2-x}Se$ size increases (Fig. 4(f)). In addition, the dual plasmonic $Au@Cu_{2-x}Se$ nanostructures exhibited exceptional catalytic durability over multiple cycles of photocatalytic reactions (Fig. S6 in the ESM). The overall morphologies of the nanoparticles were well preserved even after 3 cycles (Fig. S7 in the ESM). The photodegradation rates of monodispersed pristine $Cu_{2-x}Se$ nanoparticles were kinetically slow and the rate constant was even smaller than that of the $Au@Cu_{2-x}Se$ with the thinnest semiconductor shell, indicating the enhanced and superior performance of eccentric dual plasmonic hybrid heterostructures in photocatalysis (Fig. S13 in the ESM). To further explore the effect of plasmonic coupling and the underlying mechanism the spatial the distribution of the local electric field intensity was calculated using FDTD under sole (NIR) and dual excitations (VIS + NIR) of the LSPRs for 3 eccentric hetero-nanostructures with different $Cu_{2-x}Se$ sizes (24 nm ± 1.8 nm, 36 nm ± 2.1 nm and 54 nm ± 1.6 nm in Fig. 5(a) and histograms in Fig. S8 in the ESM). Calculations were performed at wavelengths of 840, 900, and 926 nm, corresponding to the plasmon resonances of the semiconductor, and 575 and 594 nm for the LSPRs in Au (Figs. 5(b) and 5(c)). We can clearly see that the maximal electric field intensity at the interface (shared boundary at the right

side of Au and left side of $Cu_{2-x}Se$ shells) upon NIR and dual excitations increases with $Cu_{2-x}Se$ size. The close examination reveals that all three $Au@Cu_{2-x}Se$ nanostructures under the excitation of dual LSPRs unanimously exhibit stronger local electric field enhancement ($|E/E_0|$) at the interface than that of upon sole NIR excitation. We also calculated the electric field distribution around hybrid nanostructures when Au LSPRs in the visible region are only photoexcited (Fig. S9 in the ESM).

Attributed to the plasmonic coupling between two dissimilar optical resonances, the local electric field enhancement, especially at the interface under dual simultaneous excitation is even greater than the sum of two individual excitations in which the LSPRs of Au and $Cu_{2-x}Se$ are solely photoexcited. It has been demonstrated that the formation rate of photoexcited charge carriers in semiconductors is proportional to the local intensity of the electric field [65]. The electromagnetic field enhancement due to the plasmonic coupling essentially boosts the formation rate of electron-hole pairs or excitons in semiconductors, and ultimately improves photocatalytic activity of the dual plasmonic nano-system.

Based on aforementioned results, the possible mechanism involved in the photocatalytic reactions is summarized in Fig. 4(b). Due to the Moss-Burstein effect [10], the Fermi level is closer to the edge of the valence band for p-type nonstoichiometric copper chalcogenides. The band gap values of three nano-structures including $Au@Cu_{2-x}Se\_10$ μL, $Au@Cu_{2-x}Se\_50$ μL, and $Au@Cu_{2-x}Se\_100$ μL are determined to be 1.89, 2.08, and 1.99 eV, respectively according to Tauc plots (Fig. S12 in the ESM). Abundant hydroxyl radicals can be generated from the oxidation of H_2O by the positively charged holes, which serves as a reactive oxygen species (ROS) capable of inducing the mineralization of RhB to small molecules, such as CO_2 and H_2O. Electrons diffuse into the Au core from the $Cu_{2-x}Se$ side and reduce electrophilic O_2 to superoxide radicals to drive the photocatalytic reactions, which promotes the charge separation in the excitons by suppressing the recombination rates and leads to increased hole concentration in $Cu_{2-x}Se$. The electron migration from $Cu_{2-x}Se$ to Au across the interface can be experimentally confirmed by the enhanced blue-shifted LSPRs due to the increased carrier concentration in $Cu_{2-x}Se$ during the process of photocatalytic reactions in the presence of dual plasmonic nanoparticles (Figs. S10 and S11 in the ESM). This electron transfer is also supported by other published reports [49, 58, 61]. The photocatalytic reactions can be accelerated by the synergistic plasmonic coupling between two dissimilar LSPRs by dual excitation, which produces more ROS due to the highly intensive electric filed caused by the hybridization in plasmons.

4   Conclusions

In summary, monodisperse colloidal dual plasmonic $Au@Cu_{2-x}Se$ hetero-nanostructures of eccentric form and various semi-conductor size with precisely tunable plasmonic properties have been prepared and thoroughly characterized via a facile and robust selenium-mediated two-step synthesis. Such unique nanoparticles comprising two dissimilar building blocks exhibit two characteristic LSPRs in visible and near-infrared regions that originate from the collective oscillation of free electrons and free holes in the metal and semiconductor, respectively. The photocatalytic performance of $Au@Cu_{2-x}Se$ was systematically evaluated and the decolorization process was accelerated as the size of $Cu_{2-x}Se$ increased. The rate constants of photocatalytic reactions upon dual VIS and NIR excitation were much greater than those of sole excitation (NIR) due to the plasmonic coupling between the two LSPR types. The significantly enhanced

Figure 5 The near electric field maps of the eccentric $Au@Cu_{2-x}Se$ nano-particles. (a) Schematics of the computational models of the $Au@Cu_{2-x}Se$ nanoparticles. (b) Spatial distribution of the local electric field enhance-ment ($|E/E_0|$) of the three nanoparticles excited at a single wavelength. (c) Spatial distribution of the local electric field enhancement ($|E/E_0|$) of the three nanoparticles excited at a dual wavelength. The excitation wavelengths are indicated on each panel.

strength of the electromagnetic field arising from plasmonic coupling was substantiated by the computational electrodynamic modeling. We believe the detailed understanding gained from this work provides the keystone for the practical design of dual- or even multi-plasmonic nano-systems with optimizable properties for widespread applications ranging from photo-catalysis to molecular spectroscopies.

Conflict of interest

The authors declare no competing financial interest.

Acknowledgements

Electronic Supplementary Material: Supplementary material (TEM images, measurements of interplanar spacing, extinction spectra, cycling stability, size distribution of semiconductor domains, spatial distribution of the local electric field enhancement at Au SPRs excitation wavelengths, Tauc plots for band gap determination, EDX data) is available in the online version of this article at https://doi.org/10.1007/s12274-021-3705-4.

References

[1] Willets, K. A.; Van Duyne, R. P. Localized surface plasmon resonance spectroscopy and sensing. *Annu. Rev. Phys. Chem.* **2007**, *58*, 267–297.

[2] Anker, J. N.; Hall, W. P.; Lyandres, O.; Shah, N. C.; Zhao, J.; Van Duyne, R. P. Biosensing with plasmonic nanosensors. *Nat. Mater.* **2008**, *7*, 442–453.

[3] Giannini, V.; Fernández-Domínguez, A. I.; Heck, S. C.; Maier, S. A. Plasmonic nanoantennas: Fundamentals and their use in controlling the radiative properties of nanoemitters. *Chem. Rev.* **2011**, *111*, 3888–3912.

[4] Wang, H.; Brandl, D. W.; Nordlander, P.; Halas, N. J. Plasmonic nanostructures: Artificial molecules. *Acc. Chem. Res.* **2007**, *40*, 53–62.

[5] Jain, P. K.; Huang, X. H.; El-Sayed, I. H.; El-Sayed, M. A. Noble metals on the nanoscale: Optical and photothermal properties and some applications in imaging, sensing, biology, and medicine. *Acc. Chem. Res.* **2008**, *41*, 1578–1586.

[6] Rycenga, M.; Cobley, C. M.; Zeng, J.; Li, W. Y.; Moran, C. H.; Zhang, Q.; Qin, D.; Xia, Y. N. Controlling the synthesis and assembly of silver nanostructures for plasmonic applications. *Chem. Rev.* **2011**, *111*, 3669–3712.

[7] Zhou, W.; Gao, X.; Liu, D. B.; Chen, X. Y. Gold nanoparticles for *in vitro* diagnostics. *Chem. Rev.* **2015**, *115*, 10575–10636.

[8] Comin, A.; Manna, L. New materials for tunable plasmonic colloidal nanocrystals. *Chem. Soc. Rev.* **2014**, *43*, 3957–3975.

[9] Faucheaux, J. A.; Stanton, A. L. D.; Jain, P. K. Plasmon resonances of semiconductor nanocrystals: Physical principles and new opportunities. *J. Phys. Chem. Lett.* **2014**, *5*, 976–985.

[10] Zhao, Y. X.; Pan, H. C.; Lou, Y. B.; Qiu, X. F.; Zhu, J. J.; Burda, C. Plasmonic Cu$_{2-x}$S nanocrystals: Optical and structural properties of copper-deficient copper(I) sulfides. *J. Am. Chem. Soc.* **2009**, *131*, 4253–4261.

[11] Luther, J. M.; Jain, P. K.; Ewers, T.; Alivisatos, A. P. Localized surface plasmon resonances arising from free carriers in doped quantum dots. *Nat. Mater.* **2011**, *10*, 361–366.

[12] Hsu, S. W.; On, K.; Tao, A. R. Localized surface plasmon resonances of anisotropic semiconductor nanocrystals. *J. Am. Chem. Soc.* **2011**, *133*, 19072–19075.

[13] Dorfs, D.; Härtling, T.; Miszta, K.; Bigall, N. C.; Kim, M. R.; Genovese, A.; Falqui, A.; Povia, M.; Manna, L. Reversible tunability of the near-infrared valence band plasmon resonance in Cu$_{2-x}$Se nanocrystals. *J. Am. Chem. Soc.* **2011**, *133*, 11175–11180.

[14] Kriegel, I.; Jiang, C. Y.; Rodríguez-Fernández, J.; Schaller, R. D.; Talapin, D. V.; da Como, E.; Feldmann, J. Tuning the excitonic and plasmonic properties of copper chalcogenide nanocrystals. *J. Am. Chem. Soc.* **2012**, *134*, 1583–1590.

[15] Li, W. H.; Zamani, R.; Gil, P. R.; Pelaz, B.; Ibáñez, M.; Cadavid, D.; Shavel, A.; Alvarez-Puebla, R. A.; Parak, W. J.; Arbiol, J. et al. Cu$_2$te nanocrystals: Shape and size control, plasmonic properties, and use as SERS probes and photothermal agents. *J. Am. Chem. Soc.* **2013**, *135*, 7098–7101.

[16] Xie, Y.; Carbone, L.; Nobile, C.; Grillo, V.; D'Agostino, S.; Della Sala, F.; Giannini, C.; Altamura, D.; Oelsner, C.; Kryschi, C. et al. Metallic-like stoichiometric copper sulfide nanocrystals: Phase- and shape-selective synthesis, near-infrared surface plasmon resonance properties, and their modeling. *ACS Nano* **2013**, *7*, 7352–7369.

[17] Córdova-Castro, R. M.; Casavola, M.; van Schilfgaarde, M.; Krasavin, A. V.; Green, M. A.; Richards, D.; Zayats, A. V. Anisotropic plasmonic CuS nanocrystals as a natural electronic material with hyperbolic optical dispersion. *ACS Nano* **2019**, *13*, 6550–6560.

[18] Liu, Y.; Liu, M. X.; Swihart, M. T. Plasmonic copper sulfide-based materials: A brief introduction to their synthesis, doping, alloying, and applications. *J. Phys. Chem. C* **2017**, *121*, 13435–13447.

[19] Chen, J.; Liu, T. Y.; Bao, D. Y.; Zhang, B.; Han, G.; Liu, C.; Tang, J.; Zhou, D. L.; Yang, L.; Chen, Z. G. Nanostructured monoclinic Cu$_2$Se as a near-room-temperature thermoelectric material. *Nanoscale* **2020**, *12*, 20536–20542.

[20] Min, Y.; Im, E.; Hwang, G. T.; Kim, J. W.; Ahn, C. W.; Choi, J. J.; Hahn, B. D.; Choi, J. H.; Yoon, W. H.; Park, D. S. et al. Heterostructures in two-dimensional colloidal metal chalcogenides: Synthetic fundamentals and applications. *Nano Res.* **2019**, *12*, 1750–1769.

[21] Liu, X.; Swihart, M. T. Heavily-doped colloidal semiconductor and metal oxide nanocrystals: An emerging new class of plasmonic nanomaterials. *Chem. Soc. Rev.* **2014**, *43*, 3908–3920.

[22] Manthiram, K.; Alivisatos, A. P. Tunable localized surface plasmon resonances in tungsten oxide nanocrystals. *J. Am Chem. Soc.* **2012**, *134*, 3995–3998.

[23] Ye, X. C.; Fei, J. Y.; Diroll, B. T.; Paik, T.; Murray, C. B. Expanding the spectral tunability of plasmonic resonances in doped metal-oxide nanocrystals through cooperative cation-anion codoping. *J. Am Chem. Soc.* **2014**, *136*, 11680–11686.

[24] Ye, X. C.; Hickey, D. R.; Fei, J. Y.; Diroll, B. T.; Paik, T.; Chen, J.; Murray, C. B. Seeded growth of metal-doped plasmonic oxide heterodimer nanocrystals and their chemical transformation. *J. Am. Chem. Soc.* **2014**, *136*, 5106–5115.

[25] Liu, Z. K.; Zhong, Y. X.; Shafei, I.; Jeong, S.; Wang, L. G.; Nguyen, H. T.; Sun, C. J.; Li, T.; Chen, J.; Chen, L. et al. Broadband tunable mid-infrared plasmon resonances in cadmium oxide nanocrystals induced by size-dependent nonstoichiometry. *Nano Lett.* **2020**, *20*, 2821–2828.

[26] Liu, Z. K.; Zhong, Y. X.; Shafei, I.; Borman, R.; Jeong, S.; Chen, J.; Losovyj, Y.; Gao, X. F.; Li, N.; Du, Y. P. et al. Tuning infrared plasmon resonances in doped metal-oxide nanocrystals through cation-exchange reactions. *Nat. Commun.* **2019**, *10*, 1394.

[27] Palomaki, P. K. B.; Miller, E. M.; Neale, N. R. Control of plasmonic and interband transitions in colloidal indium nitride nanocrystals. *J. Am. Chem. Soc.* **2013**, *135*, 14142–14150.

[28] Guler, U.; Shalaev, V. M.; Boltasseva, A. Nanoparticle plasmonics: Going practical with transition metal nitrides. *Mater. Today* **2015**, *18*, 227–237.

[29] Manna, G.; Bose, R.; Pradhan, N. Semiconducting and plasmonic copper phosphide platelets. *Angew. Chem., Int. Ed.* **2013**, *52*, 6762–6766.

[30] Large, N.; Abb, M.; Aizpurua, J.; Muskens, O. L. Photoconductively loaded plasmonic nanoantenna as building block for ultracompact

optical switches. *Nano Lett.* **2010**, *10*, 1741–1746.

[31] Agrawal, A.; Cho, S. H.; Zandi, O.; Ghosh, S.; Johns, R. W.; Milliron, D. J. Localized surface plasmon resonance in semiconductor nanocrystals. *Chem. Rev.* **2018**, *118*, 3121–3207.

[32] Balitskii, O. A.; Sytnyk, M.; Stangl, J.; Primetzhofer, D.; Groiss, H.; Heiss, W. Tuning the localized surface plasmon resonance in Cu$_{2−x}$Se nanocrystals by postsynthetic ligand exchange. *ACS Appl. Mater. Interfaces* **2014**, *6*, 17770–17775.

[33] Nelson, A.; Ha, D. H.; Robinson, R. D. Selective etching of copper sulfide nanoparticles and heterostructures through sulfur abstraction: Phase transformations and optical properties. *Chem. Mater.* **2016**, *28*, 8530–8541.

[34] Xu, W.; Liu, H. C.; Zhou, D. L.; Chen, X.; Ding, N.; Song, H. W.; Ågren, H. Localized surface plasmon resonances in self-doped copper chalcogenide binary nanocrystals and their emerging applications. *Nano Today* **2020**, *33*, 100892.

[35] Nikoobakht, B.; El-Sayed, M. A. Preparation and growth mechanism of gold nanorods (NRs) using seed-mediated growth method. *Chem. Mater.* **2003**, *15*, 1957–1962.

[36] Murphy, C. J.; Jana, N. R. Controlling the aspect ratio of inorganic nanorods and nanowires. *Adv. Mater.* **2002**, *14*, 80–82.

[37] Xia, X. H.; Zeng, J.; Oetjen, L. K.; Li, Q. G.; Xia, Y. N. Quantitative analysis of the role played by poly(vinylpyrrolidone) in seed-mediated growth of Ag nanocrystals. *J. Am. Chem. Soc.* **2012**, *134*, 1793–1801.

[38] Chen, J.; Wiley, B.; Li, Z. Y.; Campbell, D.; Saeki, F.; Cang, H.; Au, L.; Lee, J.; Li, X.; Xia, Y. Gold nanocages: Engineering their structure for biomedical applications. *Adv. Mater.* **2005**, *17*, 2255–2261.

[39] Jin, R. C.; Cao, Y. W.; Mirkin, C. A.; Kelly, K. L.; Schatz, G. C.; Zheng, J. G. Photoinduced conversion of silver nanospheres to nanoprisms. *Science* **2001**, *294*, 1901–1903.

[40] Chen, S. H.; Carroll, D. L. Synthesis and characterization of truncated triangular silver nanoplates. *Nano Lett.* **2002**, *2*, 1003–1007.

[41] Nehl, C. L.; Liao, H. W.; Hafner, J. H. Optical properties of star-shaped gold nanoparticles. *Nano Lett.* **2006**, *6*, 683–688.

[42] Aizpurua, J.; Hanarp, P.; Sutherland, D. S.; Käll, M.; Bryant, G. W.; de Abajo, F. J. G. Optical properties of gold nanorings. *Phys. Rev. Lett.* **2003**, *90*, 057401.

[43] Prodan, E.; Radloff, C.; Halas, N. J.; Nordlander, P. A hybridization model for the plasmon response of complex nanostructures. *Science* **2003**, *302*, 419–422.

[44] Xia, Y. N.; Halas, N. J. Shape-controlled synthesis and surface plasmonic properties of metallic nanostructures. *MRS Bull.* **2005**, *30*, 338–348.

[45] Ou, W. H.; Zou, Y.; Wang, K. W.; Gong, W. B.; Pei, R. J.; Chen, L. W.; Pan, Z. H.; Fu, D. D.; Huang, X.; Zhao, Y. F. et al. Active manipulation of NIR plasmonics: The case of Cu$_{2−x}$Se through electrochemistry. *J. Phys. Chem. Lett.* **2018**, *9*, 274–280.

[46] Jain, P. K.; Manthiram, K.; Engel, J. H.; White, S. L.; Faucheaux, J. A.; Alivisatos, A. P. Doped nanocrystals as plasmonic probes of redox chemistry. *Angew. Chem., Int. Ed.* **2013**, *52*, 13671–13675.

[47] Wei, T. X.; Liu, Y. F.; Dong, W. J.; Zhang, Y.; Huang, C. Y.; Sun, Y.; Chen, X.; Dai, N. Surface-dependent localized surface plasmon resonances in CuS nanodisks. *ACS Appl. Mater. Interfaces* **2013**, *5*, 10473–10477.

[48] Muhammed, M. A. H.; Döblinger, M.; Rodríguez-Fernández, J. Switching plasmons: Gold nanorod-copper chalcogenide core-shell nanoparticle clusters with selectable metal/semiconductor NIR plasmon resonances. *J. Am. Chem. Soc.* **2015**, *137*, 11666–11677.

[49] Kim, Y.; Park, K. Y.; Jang, D. M.; Song, Y. M.; Kim, H. S.; Cho, Y. J.; Myung, Y.; Park, J. Synthesis of Au-Cu$_2$S core-shell nanocrystals and their photocatalytic and electrocatalytic activity. *J. Phys. Chem. C* **2010**, *114*, 22141–22146.

[50] Zou, Y.; Sun, C.; Gong, W. B.; Yang, X. F.; Huang, X.; Yang, T.; Lu, W. B.; Jiang, J. Morphology-controlled synthesis of hybrid nanocrystals via a selenium-mediated strategy with ligand shielding effect: The case of dual plasmonic Au-Cu$_{2−x}$Se. *ACS Nano* **2017**, *11*, 3776–3785.

[51] Shan, B. B.; Zhao, Y. W.; Li, Y. W.; Wang, H. T.; Chen, R.; Li, M. High-quality dual-plasmonic Au@Cu$_{2−x}$Se nanocrescents with precise Cu$_{2−x}$Se domain size control and tunable optical properties in the second near-infrared biowindow. *Chem. Mater.* **2019**, *31*, 9875–9886.

[52] Li, Y. Y.; Pan, G. M.; Liu, Q. Y.; Ma, L.; Xie, Y.; Zhou, L.; Hao, Z. H.; Wang, Q. Q. Coupling resonances of surface plasmon in gold nanorod/copper chalcogenide core-shell nanostructures and their enhanced photothermal effect. *ChemPhysChem* **2018**, *19*, 1852–1858.

[53] Cui, J. B.; Jiang, R.; Guo, C.; Bai, X. L.; Xu, S. Y.; Wang, L. Y. Fluorine grafted Cu$_7$S$_4$-Au heterodimers for multimodal imaging guided photothermal therapy with high penetration depth. *J. Am. Chem. Soc.* **2018**, *140*, 5890–5894.

[54] Liu, X.; Lee, C.; Law, W. C.; Zhu, D. W.; Liu, M. X.; Jeon, M.; Kim, J.; Prasad, P. N.; Kim, C.; Swihart, M. T. Au-Cu$_{2−x}$Se heterodimer nanoparticles with broad localized surface plasmon resonance as contrast agents for deep tissue imaging. *Nano Lett.* **2013**, *13*, 4333–4339.

[55] Zhang, S. H.; Huang, Q.; Zhang, L. J.; Zhang, H.; Han, Y. B.; Sun, Q.; Cheng, Z. X.; Qin, H. Z.; Dou, S. X.; Li, Z. Vacancy engineering of Cu$_{2−x}$Se nanoparticles with tunable LSPR and magnetism for dual-modal imaging guided photothermal therapy of cancer. *Nanoscale* **2018**, *10*, 3130–3143.

[56] Ji, M. W.; Xu, M.; Zhang, W.; Yang, Z. Z.; Huang, L.; Liu, J. J.; Zhang, Y.; Gu, L.; Yu, Y. X.; Hao, W. C. et al. Structurally well-defined Au@Cu$_{2−x}$S core-shell nanocrystals for improved cancer treatment based on enhanced photothermal efficiency. *Adv. Mater.* **2016**, *28*, 3094–3101.

[57] Lv, Q.; Min, H.; Duan, D. B.; Fang, W.; Pan, G. M.; Shen, A. G.; Wang, Q. Q.; Nie, G. J.; Hu, J. M. Total aqueous synthesis of Au@Cu$_{2−x}$S core-shell nanoparticles for *in vitro* and *in vivo* SERS/PA imaging-guided photothermal cancer therapy. *Adv. Healthc. Mater.* **2019**, *8*, 1801257.

[58] Ding, X. G.; Liow, C. H.; Zhang, M. X.; Huang, R. J.; Li, C. Y.; Shen, H.; Liu, M. Y.; Zou, Y.; Gao, N.; Zhang, Z. J. et al. Surface plasmon resonance enhanced light absorption and photothermal therapy in the second near-infrared window. *J. Am. Chem. Soc.* **2014**, *136*, 15684–15693.

[59] Zhu, H.; Wang, Y.; Chen, C.; Ma, M. R.; Zeng, J. F.; Li, S. Z.; Xia, Y. S.; Gao, M. Y. Monodisperse dual plasmonic Au@Cu$_{2−x}$E (E = S, Se) core@shell Supraparticles: Aqueous fabrication, multimodal imaging, and tumor therapy at *in vivo* level. *ACS Nano* **2017**, *11*, 8273–8281.

[60] Sun, M. Q.; Fu, X. Q.; Chen, K. X.; Wang, H. Dual-plasmonic gold@copper sulfide core-shell nanoparticles: Phase-selective synthesis and multimodal photothermal and photocatalytic behaviors. *ACS Appl. Mater. Interfaces* **2020**, *12*, 46146–46161.

[61] Ma, L.; Chen, Y. L.; Yang, X.; Li, H. X.; Ding, S. J.; Hou, H. Y.; Xiong, L.; Qin, P. L.; Chen, X. B. Growth behavior of Au/Cu$_{2−x}$S hybrids and their plasmon-enhanced dual-functional catalytic activity. *CrystEngComm* **2019**, *21*, 5610–5617.

[62] Johnson, P. B.; Christy, R. W. Optical constants of the noble metals. *Phys. Rev. B* **1972**, *6*, 4370–4379.

[63] Liu, Y.; Zhu, D. W.; Hu, Y. J.; Swihart, M. T.; Wei, W. Controlled synthesis of Cu$_{2−x}$Se nanoparticles as near-infrared photothermal agents and irradiation wavelength dependence of their photothermal conversion efficiency. *Langmuir* **2018**, *34*, 13905–13909.

[64] De Ruijter, W. J.; Sharma, R.; McCartney, M. R.; Smith, D. J. Measurement of lattice-fringe vectors from digital HREM images-experimental precision. *Ultramicroscopy* **1995**, *57*, 409–422.

[65] Anger, P.; Bharadwaj, P.; Novotny, L. Enhancement and quenching of single-molecule fluorescence. *Phys. Rev. Lett.* **2006**, *96*, 113002.